

Fit-Free Optical Determination of Electronic Thermalization Time in Nematic Iron-Based Superconductors

Alexander Bartenev,¹ Roman Kolodka,¹ Ki-Tae Eom,² Jong-Hoon Kang,² Adrián Rúa-Meléndez,¹ Jason Kawasaki,² Chang-Beom Eom,² Armando Rúa,¹ and Sergiy Lysenko^{1,*}

¹*Department of Physics, University of Puerto Rico, Mayagüez, Puerto Rico 00681, USA*

²*Department of Materials Science and Engineering,
University of Wisconsin–Madison, Madison, WI 53706, USA*

We present a nematic response function model (NRFM) for fit-free direct extraction of the characteristic time of ultrafast electronic thermalization in iron-based superconductors, materials with electronic nematicity. By combining the NRFM for polarization-dependent pump–probe measurements of electronic nematic response with the two-temperature model (TTM) for sub-picosecond quasiparticle relaxation, we quantify the electronic thermalization timescales and their anisotropy. The nematic response function is modeled as the difference of normalized reflectivity signals, revealing a pronounced sub-picosecond extremum in signal evolution that directly yields the characteristic electronic thermalization time. This method demonstrates that the NRFM is consistent with TTM fits of transient optical response, yielding electronic thermalization time constants on the order of 110–230 fs for the FeSe_{1-x}Te_x and Ba(Fe_{0.92}Co_{0.08})₂As₂ thin films. The proposed approach can be applied to any material that exhibits electronic nematicity, providing a powerful tool for direct mapping of the relaxation time in nematic materials, avoiding complex experimental data-fitting procedures.

I. INTRODUCTION

Fe-based superconductors (FBSs) show a rich interplay of electronic orders [1–3], including antiferromagnetism [4], high-temperature superconductivity [5], and an electronic nematic phase that breaks rotational tetragonal symmetry without long-range magnetic order [6, 7]. FBS compounds (pnictides [8, 9] and chalcogenides [10–12]) show strongly anisotropic normal-state properties, such as in-plane resistivity [8, 10, 12] and optical conductivity [9, 11]. These observations raise the question of whether unequal coupling of spin and orbital fluctuations to the electronic fluid produces the observed in-plane transport and optical anisotropies, and they motivate ultrafast investigations of electron–electron (*e-e*) interactions and electronic contributions to magnetoelastic and nematic channels [13–15]. However, developing a reliable approach to measure the effective electron thermalization time remains challenging.

A femtosecond pump–probe experiment can drive the system out of equilibrium and track its subsequent recovery [1, 15–17]: since electrons, lattice, and spins thermalize at very different rates, one can attribute features of the transient response to specific interactions based on their characteristic times. Specifically, electronically driven nematic order [7, 18] is expected to respond on ultrafast timescales, revealing critical fluctuations that cannot be directly observed in static measurements. Moreover, the phenomenological two- and three-temperature models [14, 15, 19, 20] can be used for FBS to obtain coupling strengths among electrons, lattice, and magnetoelastic degrees of freedom.

In the optical pump–probe experiment, the time constant τ_e for the thermalization of the macroscopic electron subsystem reflects the change in the optical permittivity, averaged over *k*-space and orbitals. τ_e corresponds to the effective cooling of electrons via redistribution of spectral weight through all available channels and is sensitive to changes in collective correlations.

We also note that the information about electronic thermalization in FBSs can be obtained from ARPES measurements. ARPES can resolve d_{xz}/d_{yz} band splitting and provide *e-e* scattering rates [7, 21, 22]. However, the τ_e values obtained from optical experiments, in principle, differ somewhat from pure *e-e* scattering times obtained from ARPES. Optical experiments provide τ_e values from 0.1 up to ~ 0.5 ps [15, 23, 24], while *e-e* thermalization times from ARPES are usually shorter and strongly depend on momentum *k* and energy.

In this work, we develop a methodology to obtain the hot-electron thermalization time in nematic materials, iron-based superconductors. It uses the nematic response function model (NRFM) for polarization-resolved pump–probe signals for direct extraction of electronic relaxation time constants along two orthogonal directions of materials with electronic nematicity. We start the analysis for the case of an infinitesimally short optical pulse. Then we generalize to a finite-pulse model, where the laser pulse has a certain temporal width. We compare the determined constants with the ones obtained using the two-temperature model (TTM), revealing a close match for the average scattering time constants, as well as adding insights about anisotropies of other quasiparticle (QP) relaxation processes. Here we study the nematic dynamics of FBSs below the superconducting transition temperature T_c . The proposed approach can be applied at any temperature, provided the material exhibits electronic nematicity.

* sergiy.lysenko@upr.edu

II. NEMATIC RESPONSE FUNCTION MODEL

Transient reflectivity measurements provide insight into the carrier dynamics in a material by monitoring the time-dependent changes in reflectivity $\Delta R/R$. These changes are caused by interactions between QPs, specifically via the hot-electron thermalization followed by electron-phonon ($e-ph$) scattering. For a two-component thermalization process, the intrinsic material response can be modeled by a sum of exponential decays:

$$f(t) = Ae^{-t/\tau_e} + B \left(1 - e^{-t/\tau_{e-ph}}\right), \quad (1)$$

where A and B are the amplitudes of the reflectivity change associated with $e-e$ and $e-ph$ relaxation mechanisms, respectively, and τ_e and τ_{e-ph} are their characteristic times.

The experimentally recorded signal is the intrinsic response convolved with the instrument response function (IRF) [25, 26]:

$$\left(\frac{\Delta R}{R}\right)(t) = (\text{IRF} * f)(t) = \int_{-\infty}^{\infty} \text{IRF}(t-t') f(t') dt'. \quad (2)$$

Infinitesimally Short Pulse Excitation. In the limit of the infinitesimally short optical pulse, $\text{IRF}(t) = \delta(t)$, Eq. (2) reduces to $(\Delta R/R)(t) = f(t)$. We first derive the model in this limit, and then introduce corrections for a finite-time optical pulse.

Taking into account that the $\tau_e < \tau_{e-ph}$, at sufficiently short time scales, the term associated with $e-ph$ dynamics in Eq. (1) can be omitted: $B(1 - e^{-t/\tau_{e-ph}}) \approx 0$, and $\frac{\Delta R}{R} \approx Ae^{-t/\tau_e}$ at $t < \tau_{e-ph}$.

Measurements of the transient reflectivity at orthogonal polarizations \perp and \parallel enable observation of nematicity dynamics along orthogonal crystallographic directions. As will be shown below, the transient reflectivity signal for the two polarization channels can be modeled (at early times) by exponential decays, $(\frac{\Delta R}{R})_{\perp} = A_{\perp} \exp(-t/\tau_{\perp})$ and $(\frac{\Delta R}{R})_{\parallel} = A_{\parallel} \exp(-t/\tau_{\parallel})$, where A_{\perp} and A_{\parallel} are the amplitudes of the reflectivity change and τ_{\perp} and τ_{\parallel} are the characteristic electronic thermalization times for each polarization channel. The time difference $\Delta\tau = \tau_{\perp} - \tau_{\parallel}$ is assumed to be relatively small.

The nematic response function can be constructed as

$$\tilde{\eta} = (\Delta R/R)_{\parallel} - (\Delta R/R)_{\perp}. \quad (3)$$

By renormalizing it as $\eta = \frac{\tilde{\eta}}{A_{\perp}}$ with amplitude ratio $r = \frac{A_{\parallel}}{A_{\perp}}$, we obtain

$$\eta = r \cdot \exp(-t/\tau_{\parallel}) - \exp(-t/\tau_{\perp}). \quad (4)$$

This function has one extremum. For $\Delta\tau > 0$, this extremum is a minimum. Its position t_{\min} can be obtained

by solving the $\frac{d\eta}{dt}(t_{\min}) = 0$. Assuming $\Delta\tau \ll \tau_{\parallel}, \tau_{\perp}$,

$$t_{\min} \approx \tau_{\parallel} + \frac{\Delta\tau}{2} + \ln(r) \left(\tau_{\parallel} + \frac{\tau_{\parallel}^2}{\Delta\tau} \right). \quad (5)$$

In case of equal amplitudes $A_{\perp} = A_{\parallel}$, $r = 1$ and $\ln(r) = 0$ we obtain

$$t_{\min} \approx \tau_{\parallel} + \frac{\Delta\tau}{2} = \frac{\tau_{\perp} + \tau_{\parallel}}{2} = \tau_{\text{avg}}. \quad (6)$$

This result indicates that the temporal position of the nematicity signal η minimum (or maximum) corresponds to the average relaxation time τ_{avg} of the material.

The nematic response function was modeled for various τ_{\perp} and τ_{\parallel} and is presented on Fig. 1(a), where the maximum difference between t_{\min} and τ_{avg} is less than 2 fs ($\tau_{\text{avg}}=110$ fs, $t_{\min}=108.6$ fs) for $\Delta\tau=30$ fs with $\tau_{\parallel}=95$ fs and $\tau_{\perp}=125$ fs. The position of the minimum t_{\min} of the nematic response function modeled for the $\tau_{\parallel} = 95$ fs and $\tau_{\perp} = 96 - 125$ fs is shown in Fig. 1(b), indicating close match between actual τ_{avg} and t_{\min} , in agreement with Eq. (6).

Furthermore, the value of the nematic response function in the minimum can be used to estimate the difference between electronic thermalization time constants for two directions. In case of $r = 1$, the expansion of the normalized nematic response function around t_{\min} yields its amplitude η_{\min} at the minimum position: $\eta_{\min} \approx -\frac{\Delta\tau}{e \cdot t_{\min}}$. Therefore, the difference $\Delta\tau$ between electronic thermalization times for two directions associated with maximal nematic response can be estimated as

$$\Delta\tau \approx -e \cdot \eta_{\min} \cdot t_{\min}. \quad (7)$$

We note that, in Eq. (5), t_{\min} diverges for $\Delta\tau \rightarrow 0$ and $\ln(r) \neq 0$, as shown in Fig. 1(c). Therefore, to obtain t_{\min} with higher accuracy, it is important to renormalize the experimental data to enforce equal amplitudes $A_{\perp} = A_{\parallel}$, leading to $r = 1$ and $\ln(r) = 0$. We note that it is also convenient to rescale the amplitudes to unity, $A_{\perp} = A_{\parallel} = 1$, without loss of generality. If the data are not normalized, the amplitude differences can cause errors between actual t_{\min} and approximated $t_{\min} \approx \tau_{\text{avg}}$ [Fig. 1(c)]. The error increases with the decreasing $\Delta\tau$. By combining (6) and (7), it is possible to identify both τ_{\parallel} and τ_{\perp} as

$$\tau_{\parallel, \perp} \approx t_{\min} \left(1 \pm \frac{1}{2} e \cdot \eta_{\min}\right). \quad (8)$$

Equations (7) and (8), applied to extract electronic thermalization time from the transient reflectivity data will hereafter be referred to as the *nematic response function model* (NRFM).

Finite-Pulse Excitation. For a finite duration of optical pulse, the experimentally recorded transient is the convolution of the intrinsic material response with the IRF [26]. For Gaussian pump and probe pulses of equal duration τ_p at the full width at half maximum (FWHM), the IRF is also Gaussian, with FWHM $\tau_{\text{IRF}} = \sqrt{2} \tau_p$.

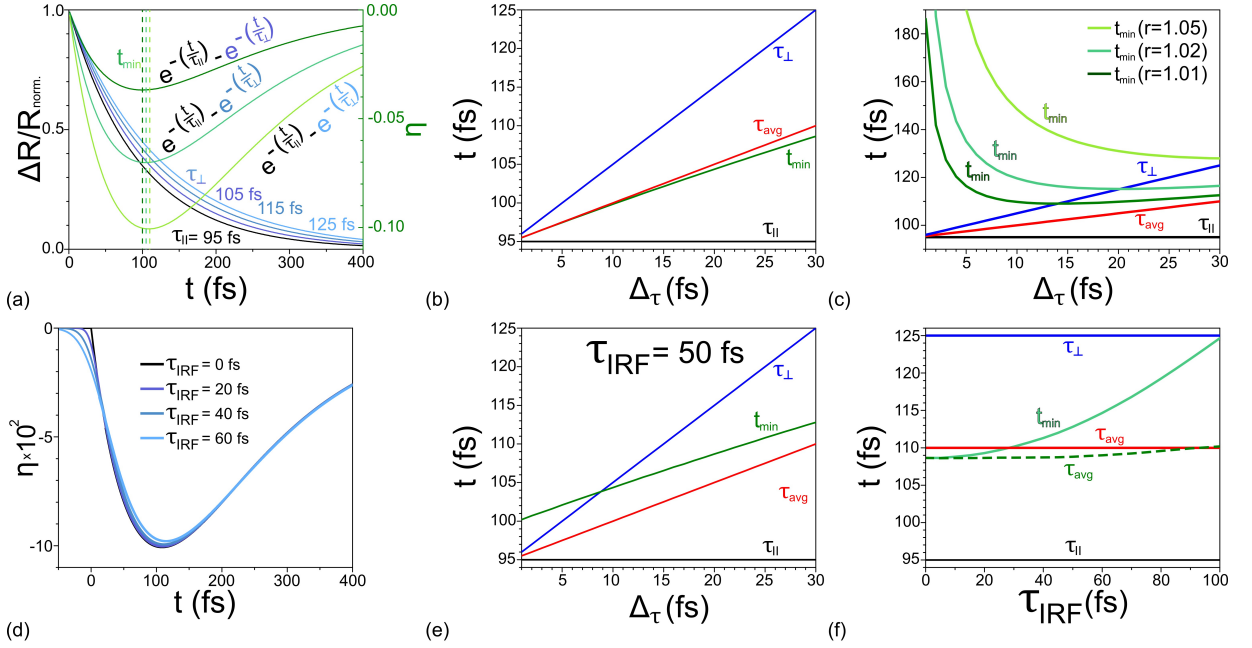


FIG. 1. Nematic response function model. (a) Modeling of transient nematicity signal η as a difference of normalized exponential decay functions $\exp(-t/\tau_{\parallel,\perp})$ with characteristic relaxation times $\tau_{\parallel} = 95$ fs and $\tau_{\perp} = 105, 115,$ and 125 fs for the infinitesimally short optical excitation ($\tau_{\text{IRF}} = 0$ fs). (b) Minimum position t_{min} versus $\Delta\tau$, compared to τ_{\perp} , τ_{\parallel} and their average τ_{avg} for $\tau_{\text{IRF}} = 0$ fs. (c) Divergence of t_{min} at small $\Delta\tau$ when $\ln(r) \neq 0$ ($r = 1.01, 1.02, 1.05$), and $\tau_{\text{IRF}} = 0$ fs. (d) Modeling of η for finite-pulse excitation with $\tau_{\text{IRF}} = 0 - 60$ fs: difference of exponentials $\exp(-t/\tau_{\parallel,\perp})$ convolved with a Gaussian IRF ($\tau_{\parallel} = 95$ fs, $\tau_{\perp} = 125$ fs). (e) t_{min} versus $\Delta\tau$ with a Gaussian IRF, compared to τ_{\perp} , τ_{\parallel} , and τ_{avg} ($\tau_{\text{IRF}} = 50$ fs). (f) Comparison between the modeled τ_{avg} (solid line), the minimum position t_{min} , and the τ_{avg} (dashed line) calculated from Eq. (17).

The renormalized ($A = 1$) intrinsic response is defined as

$$f(t; \tau_e) = \begin{cases} 1, & t < 0, \\ e^{-t/\tau_e}, & t \geq 0, \end{cases} \quad (9)$$

and the measured trace as $F(t; \tau_e) = (g * f)(t)$. The IRF can be approximated by a Gaussian of FWHM τ_{IRF} [26, 27]:

$$g(t) = \frac{\kappa}{\sqrt{2\pi} \tau_{\text{IRF}}} \exp\left[-\frac{\kappa^2 t^2}{2\tau_{\text{IRF}}^2}\right], \quad (10)$$

where $\kappa = 2\sqrt{2\ln 2}$. The convolution can be evaluated as

$$F(t; \tau_e) = (g * f)(t) = 1 - \Phi\left(\frac{\kappa t}{\tau_{\text{IRF}}}\right) + S(t; \tau_e, \tau_{\text{IRF}}), \quad (11)$$

where $\Phi(x)$ is the standard normal cumulative distribution function [28]

$$\Phi(x) = \frac{1}{2} \left[1 + \text{erf}\left(\frac{x}{\sqrt{2}}\right) \right] \quad (12)$$

and $S(t; \tau_e, \tau_{\text{IRF}})$ is

$$S(t; \tau_e, \tau_{\text{IRF}}) = \exp\left[\frac{\tau_{\text{IRF}}^2}{2\kappa^2\tau_e^2} - \frac{t}{\tau_e}\right] \Phi\left(\frac{\kappa t}{\tau_{\text{IRF}}} - \frac{\tau_{\text{IRF}}}{\kappa\tau_e}\right). \quad (13)$$

The nematic response function is

$$\eta(t) = F(t; \tau_{\parallel}) - F(t; \tau_{\perp}). \quad (14)$$

Figure 1(d) shows a comparison of $\eta(t)$ obtained for different IRFs by numerical simulation. Thus, the finite width of the optical pulse reduces the minimum amplitude η_{min} and shifts $t_{\text{min}}(\Delta\tau)$ shown in Fig. 1(b) for $\tau_{\text{IRF}} = 0$ fs to longer delays of several femtoseconds, as shown in Fig. 1(e) for $\tau_{\text{IRF}} = 50$ fs. Although the difference between τ_{avg} and t_{min} increases, it remains below 5 fs, indicating that for $\tau_{\text{IRF}} = 50$ fs the infinitesimally short pulse approximation remains valid.

For $|\Delta\tau| \ll \tau_{\text{avg}}$, $\eta(t)$ expanded around the mean relaxation time $\tau_{\text{avg}} = (\tau_{\parallel} + \tau_{\perp})/2$ to obtain

$$\eta(t) \approx -\Delta\tau \partial_{\tau_{\text{avg}}} S(t; \tau_{\text{avg}}, \tau_{\text{IRF}}). \quad (15)$$

Solving $d\eta/dt = 0$ for $\kappa \tau_{\text{avg}}/\tau_{\text{IRF}} > 3$ yields

$$t_{\text{min}} \approx \tau_{\text{avg}} + \frac{\tau_{\text{IRF}}^2}{\kappa^2 \tau_{\text{avg}}} \quad \left(\frac{\kappa \tau_{\text{avg}}}{\tau_{\text{IRF}}} > 3\right). \quad (16)$$

This leads to IRF-corrected NRFM relations (a detailed derivation is provided in the Supplementary Material):

$$\tau_{\text{avg}} \approx t_{\text{min}} - \frac{\tau_{\text{IRF}}^2}{\kappa^2 t_{\text{min}}}, \quad (17)$$

$$\Delta\tau \approx -e \eta_{\text{min}} \tau_{\text{avg}} \exp\left(\frac{\tau_{\text{IRF}}^2}{2\kappa^2 \tau_{\text{avg}}^2}\right), \quad (18)$$

$$\tau_{\parallel,\perp} \approx \tau_{\text{avg}} \mp \frac{\Delta\tau}{2}. \quad (19)$$

Equation (16) shows that a finite time resolution τ_{IRF} shifts the minimum to longer delays, with a quadratic dependence on τ_{IRF} . As shown in Fig. 1(f), applying Eq. (17) accounts for this shift and yields accurate τ_{avg} even when $\tau_{\text{avg}} \approx \tau_{\text{IRF}}$.

Two-Temperature Model. The carrier and lattice dynamics can also be analyzed by the widely used TTM [29, 30], which describes the temperature evolution of electrons T_e and the lattice T_L after a photoexcitation as

$$C_e(T_e) \frac{\partial T_e(t)}{\partial t} = -G(T_e(t) - T_L(t)) + S(\tau_e, t) \quad (20)$$

$$C_L(T_L) \frac{\partial T_L(t)}{\partial t} = G(T_e(t) - T_L(t)), \quad (21)$$

where G is the e - ph coupling constant, $C_e(T_e)$ and $C_L(T_L)$ are the electronic and lattice heat capacities per unit volume, respectively. The electronic heat capacity is a linear function of T_e : $C_e(T_e) = \gamma T_e$ and γ is a Sommerfeld coefficient that depends on the density of states at the Fermi level [31]. The term $S(\tau_e, t)$ is a modified source term that accounts for non-instantaneous electron thermalization, defined by τ_e [32]:

$$S(t) = \frac{0.94(1-R)}{(\tau_p + \tau_e)d} F \left(1 - e^{-\frac{t}{\delta}}\right) e^{\left[-2.77\left(\frac{t-2(\tau_p+\tau_e)}{\tau_p+\tau_e}\right)^2\right]} \quad (22)$$

where F is the laser fluence, d is the film thickness, and δ is the optical penetration depth. Transient reflectivity response can be modeled from the obtained electron and lattice temperatures:

$$\frac{\Delta R}{R}(t) = a\Delta T_e(t) + b\Delta T_L(t) \quad (23)$$

where a and b are the fitting parameters, $\Delta T_e(t) = T_e(t) - T_e(0)$ and $\Delta T_L(t) = T_L(t) - T_L(0)$. Eq. (23) can be used when the excitation remains reversible (i.e., below ablation/damage) [14]. While the fluences used in this work (up to 8 mJ/cm²) are higher than in previous works [13, 14], they are still well below 25 mJ/cm², whereat which the lattice temperature on a thin film surface can transiently exceed the melting temperature [35].

In this work, the two methodologies, NRFM and TTM, focus on different aspects: NRFM directly estimates τ_e from the nematic (anisotropic) signal at early times $t < \tau_{e-ph}$, whereas TTM fits the reflectivity signal, where the τ_e and G are fitting parameters. By comparing the results, we can check for consistency and probe anisotropy in other relaxation channels, not addressed by TTM.

III. METHODS

Samples. Epitaxial 40-nm-thick FeSe_{0.8}Te_{0.2} and 190-nm-thick FeSe films were deposited on CaF₂ single-crystal substrates by pulsed laser deposition (PLD) at

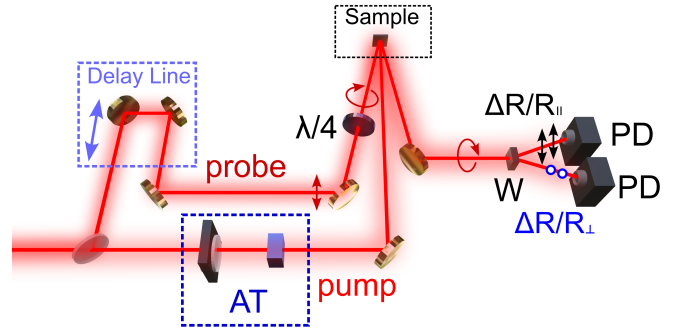


FIG. 2. Schematic of the experimental setup for polarization-resolved pump-probe measurements. AT is pump intensity attenuator, $\lambda/4$ is quarter-wavelength plate, W is a Wollaston prism, and PD are photodetectors.

10⁻⁶ Torr by Lambda Physik Compex 110 excimer laser with 1.5 J/cm² fluence. During the deposition process, the substrate temperature was fixed at 573 K. Optimally doped 80-nm-thick Ba(Fe_{1-x}Co_x)₂As₂ ($x = 0.08$) films were grown by PLD on (La, Sr)(Al, Ta)O₃ [LSAT] and LaAlO₃ [LAO] single-crystalline substrates with an epitaxial SrTiO₃ [STO] template buffer layer. STO template was etched by buffered hydrofluoric acid to achieve TiO₂ terminated surface.

Optical Measurements. In pump-probe measurements, we used the Spectra-Physics Ti:Sapphire femtosecond laser system with a pulse duration of $\tau_p = 35$ fs, 800 nm central wavelength, and 1 kHz repetition rate. The pump-probe experiments were carried out in reflection geometry (Fig. 2), with the adjustable pump fluence up to 8 mJ/cm². The pump and probe pulses were overlapped on the sample surface, with substantially reduced intensity of probe pulses to avoid nonlinear interaction with the sample. The instrument time constant for 35 fs optical pulses is $\tau_{\text{IRF}} \approx 50$ fs. An electromechanical optical delay line controlled the time delay between pump and probe. The pump beam passed through the computer-controlled attenuator, enabling the precise control of the pump fluence. A circularly polarized probe was used for nematicity measurements. The circularity of the probe pulse was detected using a Wollaston prism. Samples were enclosed in an optical cryostat with a minimum possible temperature of 3 K.

Two polarization channels are recorded simultaneously using gains that provide equal amplitudes at the maximum of the transient signal. Gain balancing resulted in the relative scaling of the factor $r \equiv A_{\parallel}/A_{\perp}$, as close to unity as possible. The remaining small deviation $r \neq 1$ due to sensitivity drift, differences in optical losses, or noise was eliminated by post-processing via a simple linear renormalization of a channel by a constant factor, making $A_{\parallel} = A_{\perp}$. This renormalization is equivalent to choosing a common measurement scale. It does not change the shape of the normalized nematicity function $\eta(t)$ and, hence, the position of its extremum at t_{min} . We note that the renormalization procedure does not intro-

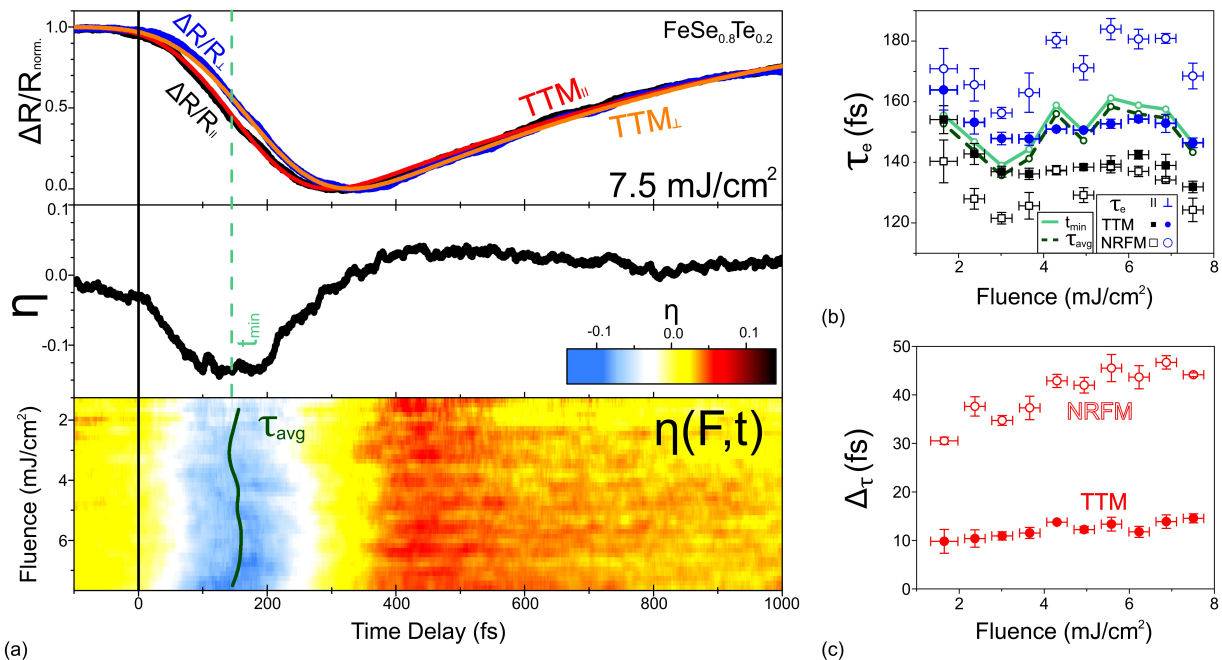


FIG. 3. (a) Subpicosecond transient reflectivity of $\text{FeSe}_{0.8}\text{Te}_{0.2}$ at 8 K. Top panel: normalized transient reflectivity with superimposed TTM fits. Middle panel: nematic response function η for transient reflectivity traces, shown in the top panel. Bottom panel: 2D map of the nematic response function η versus photoexcitation fluence and time delay. Solid line near the minimum $\eta_{\min}(F, t_{\min})$ corresponds to τ_{avg} from Eq. (17). (b) Electronic thermalization time constants, obtained from TTM (solid) and NRMF (hollow). Solid and dashed lines show t_{\min} and τ_{avg} from Eq. (17), respectively. (c) Differences $\Delta\tau$, obtained from (b).

duce additional fitting parameters and does not affect the extracted characteristic time, defined by the time marker t_{\min} .

IV. RESULTS AND DISCUSSION

The ultrafast pump-probe measurements were performed for three samples: (i) $\text{FeSe}_{0.8}\text{Te}_{0.2}$ epitaxial film at $T = 8$ K, (ii) FeSe film at $T = 3$ K, and (iii) $\text{Ba}(\text{Fe}_{0.92}\text{Co}_{0.08})_2\text{As}_2$ at $T = 8$ K.

Figure 3(a) shows the transient reflectivity of $\text{FeSe}_{0.8}\text{Te}_{0.2}$. A sharp initial signal drop is attributed to hot-electron thermalization, followed by an increase attributed to the redistribution of excitation energy between electrons and lattice. The pronounced difference between normalized transient reflectivities along the two orthogonal directions results in photoinduced nematic response $\eta(t)$. This function has a pronounced minimum at $t_{\min} \approx 150$ fs. The determination of τ_{avg} here is based on the temporal position t_{\min} of the extremum $\eta(t)$, but not on the absolute amplitude of the signal [Eq. (17)]. The normalization of the channels as $A_{\parallel} = A_{\perp} = 1$ with $r \rightarrow 1$ changes only the vertical scale of $\eta(t)$ and does not lead to a shift of t_{\min} .

Since t_{\min} is obtained from a position of local extremum $\eta(t)$ rather than from a multi-parameter fit, the reliability of t_{\min} determination is high and is controlled

by a few factors, such as (i) the signal-to-noise ratio near the extremum, (ii) baseline drift and normalization, (iii) the accuracy of the zero-time determination, and (iv) the width of the instrument response function $\text{IRF}(t)$. The extraction of τ_{avg} from t_{\min} assumes that the analysis window is limited to early times when electron thermalization dominates ($t < \tau_{e-ph}$). For accurate anisotropy extraction, the amplitudes must be aligned, making $r \rightarrow 1$. Otherwise, a possible amplitude mismatch can introduce a bias in t_{\min} in the limit of small $\Delta\tau$ [see Fig. 1(c)].

Figure 3(b) shows that the TTM fitting yields electronic thermalization time constants τ_e that closely match the NRMF-derived time constants τ_{avg} and $\tau_{\parallel,\perp}$ using Eqs. (17) and (19), respectively, revealing that both methods are capturing the same physical timescale. One can see the good agreement between NRMF (hollow points) and TTM (solid lines) – the two sets of values are close to each other for all fluences. This consistency across a wide range of pump fluences validates the NRMF approach as a reliable method to obtain τ_e using the nematic signal alone. It also suggests that the modified TTM, which includes a finite τ_e , is appropriately modeling the initial electronic excitation.

Figure 3(c) shows the $\Delta\tau$ values obtained using both models, TTM and NRMF [Eq. (18)]. The models predict the same fluence-dependent behavior of the differences $\Delta\tau$ qualitatively. NRMF provides higher values of

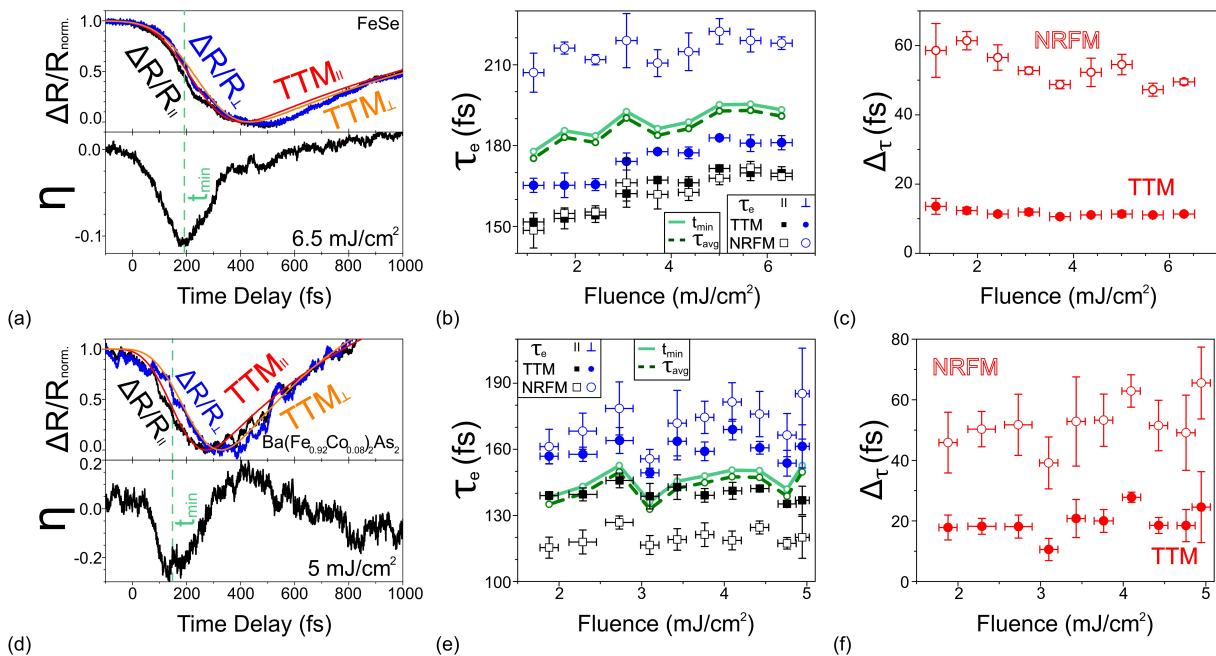


FIG. 4. Subpicosecond transient dynamics of FeSe and $\text{Ba}(\text{Fe}_{0.92}\text{Co}_{0.08})_2\text{As}_2$. (a) Top panel: normalized transient reflectivity of FeSe thin film at 3 K with superimposed TTM fits. Bottom panel: nematic response function η for transient reflectivity traces, shown in the top panel. (b) Electronic thermalization time constants, obtained from TTM (solid) and from NRFM (hollow), for FeSe thin film. Solid and dashed lines show t_{\min} and the τ_{avg} obtained from Eq. (17), respectively. (c) Differences $\Delta\tau$, obtained from (b). (d) Top panel: normalized transient reflectivity of $\text{Ba}(\text{Fe}_{0.92}\text{Co}_{0.08})_2\text{As}_2$ thin film at 8 K with superimposed TTM fits. Bottom panel: nematic response function η for transient reflectivity traces, shown in the top panel. (e) Electronic thermalization time constants, obtained from TTM (solid) and from NRFM (hollow), for $\text{Ba}(\text{Fe}_{0.92}\text{Co}_{0.08})_2\text{As}_2$ thin film. Solid and dashed lines show t_{\min} and τ_{avg} from Eq. (17), respectively. (f) Differences $\Delta\tau$, obtained from (e).

$\Delta\tau$. The observed discrepancy can originate from the differences in approximations for each model.

The subpicosecond transient response of FeSe thin film is similar to observed dynamics of $\text{FeSe}_{0.8}\text{Te}_{0.2}$. Notably, the modified TTM fits the dynamics of FeSe thin film less accurately (the coefficient of determination \mathfrak{R}^2 of the fits $\geq 96\%$) than the $\text{FeSe}_{0.8}\text{Te}_{0.2}$ ($\mathfrak{R}^2 \geq 98\%$), as seen in Fig. 4(a), where the modified TTM does not match the initial drop and subsequent rise as good as for $\text{FeSe}_{0.8}\text{Te}_{0.2}$ [Fig. 3(a)]. It could be caused by a more pronounced nematic phase that Te doping suppresses: $T_s = 90$ K for undoped sample, temperature of structural transition reduces to $T_s = 60$ K for $\text{FeSe}_{0.8}\text{Te}_{0.2}$, structural transition completely vanishes for $\text{FeSe}_{0.5}\text{Te}_{0.5}$ [2].

The electronic thermalization constants τ_e , obtained using both methods, show good match, with NRFM predicting higher τ_{\perp} [Fig. 4(b)] and $\Delta\tau$ [Fig. 4(c)]. Notably, the divergence of $\Delta\tau$ decreases with the fluence increase for FeSe, while increasing for $\text{FeSe}_{0.8}\text{Te}_{0.2}$. The origin of this divergence remains unclear and requires future investigation of the QP dynamics in these materials. Although the agreement between NRFM and TTM is less for FeSe than for $\text{FeSe}_{0.8}\text{Te}_{0.2}$ (both for τ_e and $\Delta\tau$), the extracted mean value τ_{avg} lies within one pulse width τ_p of both τ_{\perp} and τ_{\parallel} .

The subpicosecond dynamics of optimally doped

$\text{Ba}(\text{Fe}_{0.92}\text{Co}_{0.08})_2\text{As}_2$ thin film [Fig. 4(d)] is similar to the chalcogenides (FeSe and $\text{FeSe}_{0.8}\text{Te}_{0.2}$). For $\text{Ba}(\text{Fe}_{0.92}\text{Co}_{0.08})_2\text{As}_2$ [Fig. 4(e)], the electronic thermalization time constant τ_e does not show a clear fluence dependence and both models yield comparable values. The τ_e values differ by only $\sim \tau_p$, i.e., within the experimental time resolution. The extracted $\Delta\tau$ values [Fig. 4(f)] differ more between the models, but the discrepancy is still on the order of the pulse duration.

Overall, the mean values τ_{avg} obtained from NRFM are consistent with the τ_e values from TTM within the pulse duration and in agreement with typical values obtained for FBSs [15, 23, 24]. Moreover, the IRF correction to τ_{avg} (~ 3 fs in this work) is much smaller than the pulse duration and can be neglected. Thus, the NRFM approximation of infinitesimally short optical pulse excitation with $\tau_{\text{IRF}} = 0$ fs, where $\tau_{\text{avg}} \approx t_{\min}$, is sufficient. Additionally, these approximation errors are systematic and therefore do not affect the predicted relative trends. To reduce uncertainties associated with the finite IRF, one can use shorter optical pulses.

According to Gurzhi's theory [33, 34], one can expect a noticeable decrease in τ_e with increasing pump fluence. However, τ_e shows a weak dependence on the excitation level for FBSs in the superconducting regime: a slight decrease in τ_e vs pump level is observed only for

FeSe_{0.8}Te_{0.2} [Fig. 3(b)], while for Ba(Fe_{0.92}Co_{0.08})₂As₂ almost no dependence on the pump fluence was detected [Fig. 4(e)]. An unexpected growth in τ_e with increasing pump fluence is noteworthy for FeSe [Fig. 4(b)]. Such unusual behaviors are associated with specific photoinduced dynamics of QPs and Cooper pair breakdown on sub-ps time scales in superconducting regime. We also note that the preliminary studies of τ_e showed that the trend of τ_e vs pump fluence changes above T_c . Therefore, temperature-dependent studies of $\tau_e(F)$ are promising for understanding the nature of superconductivity in FBSs.

The times τ_{avg} , τ_{\perp} , and τ_{\parallel} extracted by NRFM should be understood here as the characteristic times of electron thermalization of the quasi-equilibrium electron subsystem, observed through the ultrafast evolution of the nematic optical response $\eta(t)$, rather than as the direct microscopic time of single e - e scattering. Extracted time shows how quickly the electron subsystem, after photoexcitation, relaxes to a quasi-thermal distribution and can include the contribution of several fast processes (e.g., energy redistribution within the electron band, relaxation of the distribution anisotropy, and ultrafast nematic channels). This time is somewhat different from the e - e scattering time determined by ARPES, which pertains to a more microscopic time scale of electron state broadening, and depends on the specific definition of the observable. Therefore, here τ_{avg} , τ_{\perp} , and τ_{\parallel} are integral measures of the electron thermalization rate, directly accessible from optical experiments.

V. CONCLUSION

In summary, a robust methodology based on polarization-resolved transient reflectivity measurements was developed for direct extraction of ultrafast electronic thermalization times in iron-based superconductors with electronic nematicity. The agreement between the time constants obtained by NRFM and independent TTM analysis confirms the consistency of the approach. The electronic thermalization time constants obtained for Ba(Fe_{0.92}Co_{0.08})₂As₂ and FeSe_{1-x}Te_x by using NRFM

show good agreement with time constants obtained from the widely used TTM.

An important advantage of NRFM is that the electronic thermalization time is extracted from a stable time marker t_{min} for the extremum of the nematicity function η . This makes the procedure insensitive to the choice of fitting parameters as compared to global multi-exponential or TTM approaches. Therefore, the NRFM method is well suited for high-throughput analysis of relaxation trends as a function of temperature, doping, or fluence. The proposed nematic response function model offers a quantitative probe of anisotropic electron dynamics not only for iron-based superconductors but also for a broad class of correlated materials with electronic nematicity, enabling quantification of the photoinduced dynamics of the nematic state.

SUPPLEMENTARY MATERIAL

See the supplementary material for corrections to the nematic response function model that account for the finite time resolution of the experiment.

ACKNOWLEDGMENTS

The authors gratefully acknowledge support from the U.S. Army Research Office, accomplished under Grant Number W911NF-25-1-0122, and from the National Science Foundation, Awards #2425113 and #1905691. CBE acknowledges support for this research through a Vannevar Bush Faculty Fellowship (ONR N00014-20-1-2844), and the Gordon and Betty Moore Foundation's EPiQS Initiative, Grant GBMF9065. Thin film synthesis and transport measurements at the University of Wisconsin–Madison were supported by the U.S. Department of Energy (DOE), Office of Science, Office of Basic Energy Sciences (BES), under award number DE-FG02-06ER46327. The authors gratefully acknowledge partial support of this research by NSF through the University of Wisconsin Materials Research Science and Engineering Center (DMR-2309000).

-
- [1] D. H. Torchinsky, J. W. McIver, D. Hsieh, G. Chen, J. Luo, N. Wang, and N. Gedik, "Nonequilibrium quasiparticle relaxation dynamics in single crystals of hole- and electron-doped BaFe₂As₂," *Phys. Rev. B* **84**, 104518 (2011).
- [2] K. Mukasa, K. Matsuura, M. Qiu, M. Saito, Y. Sugimura, K. Ishida, M. Otani, Y. Onishi, Y. Mizukami, K. Hashimoto, *et al.*, "High-pressure phase diagrams of FeSe_{1-x}Te_x: correlation between suppressed nematicity and enhanced superconductivity," *Nat. Commun.* **12**, 381 (2021).
- [3] A. Lucarelli, A. Dusza, F. Pfuner, P. Lerch, J. G. Analytis, J.-H. Chu, I. R. Fisher, and L. Degiorgi, "Charge dynamics of Co-doped BaFe₂As₂," *New J. Phys.* **12**, 073036 (2010).
- [4] Y. Su, P. Link, A. Schneidewind, T. Wolf, P. Adelman, Y. Xiao, M. Meven, R. Mittal, M. Rotter, D. Johrendt, *et al.*, "Antiferromagnetic ordering and structural phase transition in Ba₂Fe₂As₂ with Sn incorporated from the growth flux," *Phys. Rev. B* **79**, 064504 (2009).
- [5] D. Liu, W. Zhang, D. Mou, J. He, Y.-B. Ou, Q.-Y. Wang, Z. Li, L. Wang, L. Zhao, S. He, *et al.*, "Electronic origin of high-temperature superconductivity in single-layer FeSe superconductor," *Nat. Commun.* **3**, 931 (2012).
- [6] L. W. Harriger, H. Luo, M. Liu, C. Frost, J. Hu, M. Norman, and P. Dai, "Nematic spin fluid in the tetragonal phase of BaFe₂As₂," *Phys. Rev. B* **84**, 054544 (2011).

- [7] T. Shimojima, Y. Suzuki, A. Nakamura, N. Mitsuishi, S. Kasahara, T. Shibauchi, Y. Matsuda, Y. Ishida, S. Shin, and K. Ishizaka, “Ultrafast nematic-orbital excitation in FeSe,” *Nat. Commun.* **10**, 1946 (2019).
- [8] M. He, L. Wang, F. Ahn, F. Hardy, T. Wolf, P. Adelmann, J. Schmalian, I. Eremin, and C. Meingast, “Dichotomy between in-plane magnetic susceptibility and resistivity anisotropies in extremely strained BaFe₂As₂,” *Nat. Commun.* **8**, 504 (2017).
- [9] M. Nakajima, T. Liang, S. Ishida, Y. Tomioka, K. Kihou, C. Lee, A. Iyo, H. Eisaki, T. Kakeshita, T. Ito, *et al.*, “Unprecedented anisotropic metallic state in undoped iron arsenide BaFe₂As₂ revealed by optical spectroscopy,” *Proc. Natl. Acad. Sci. USA* **108**, 12238–12242 (2011).
- [10] J. M. Bartlett, A. Steppke, S. Hosoi, H. Noad, J. Park, C. Timm, T. Shibauchi, A. P. Mackenzie, and C. W. Hicks, “Relationship between transport anisotropy and nematicity in FeSe,” *Phys. Rev. X* **11**, 021038 (2021).
- [11] M. Chinotti, A. Pal, L. Degiorgi, A. E. Böhmer, and P. C. Canfield, “Ingredients for the electronic nematic phase in FeSe revealed by its anisotropic optical response,” *Phys. Rev. B* **98**, 094506 (2018).
- [12] M. A. Tanatar, A. E. Böhmer, E. I. Timmons, M. Schütt, G. Drachuck, V. Taufour, K. Kothapalli, A. Kreyssig, *et al.*, “Origin of the resistivity anisotropy in the nematic phase of FeSe,” *Phys. Rev. Lett.* **117**, 127001 (2016).
- [13] T. Konstantinova, L. Wu, M. Abeykoon, R. Koch, A. Wang, R. Li, X. Shen, J. Li, J. Tao, I. Zaliznyak, *et al.*, “Photoinduced dynamics of nematic order parameter in FeSe,” *Phys. Rev. B* **99**, 180102 (2019).
- [14] B. Mansart, D. Boschetto, A. Savoia, F. Rullier-Albenque, F. Bouquet, E. Papalazarou, A. Forget, D. Colson, A. Rousse, and M. Marsi, “Ultrafast transient response and electron-phonon coupling in the iron-pnictide superconductor Ba(Fe_{1-x}Co_x)₂As₂,” *Phys. Rev. B* **82**, 024513 (2010).
- [15] A. Patz, T. Li, S. Ran, R. M. Fernandes, J. Schmalian, S. L. Bud’ko, P. C. Canfield, I. E. Perakis, and J. Wang, “Ultrafast observation of critical nematic fluctuations and giant magnetoelastic coupling in iron pnictides,” *Nat. Commun.* **5**, 3229 (2014).
- [16] D. H. Torchinsky, G. F. Chen, J. L. Luo, N. L. Wang, and N. Gedik, “Band-dependent Quasiparticle Dynamics in Single Crystals of the Ba_{0.6}K_{0.4}Fe₂As₂ Superconductor Revealed by Pump-Probe Spectroscopy,” *Phys. Rev. Lett.* **105**, 027005 (2010).
- [17] X. Yang, L. Luo, M. Mootz, A. Patz, S. L. Bud’ko, P. Canfield, I. Perakis, and J. Wang, “Nonequilibrium pair breaking in Ba(Fe_{1-x}Co_x)₂As₂ superconductors: evidence for formation of a photoinduced excitonic state,” *Phys. Rev. Lett.* **121**, 267001 (2018).
- [18] C.-W. Luo, P. C. Chung, S.-H. Wang, J.-C. Chiang, J.-Y. Lin, K.-H. Wu, J.-Y. Juang, D. A. Chareev, O. S. Volkova, and A. N. Vasiliev, “Unveiling the hidden nematicity and spin subsystem in FeSe,” *npj Quantum Materials* **2**, 32 (2017).
- [19] L. Rettig, R. Cortés, H. S. Jeevan, P. Gegenwart, T. Wolf, J. Fink, and U. Bovensiepen, “Electron–phonon coupling in 122 Fe pnictides analyzed by femtosecond time-resolved photoemission,” *New J. Phys.* **15**, 083023 (2013).
- [20] A. Bartenev, R. S. Kolodka, C. Verbel, A. Rua, L. Theran, F. Fernandez, A. Rua, and S. Lysenko, “Structural transition dynamics in FeSe_{0.8}Te_{0.2} thin film,” in *Laser Science*, paper LW5F-4 (2023).
- [21] M. D. Watson, T. K. Kim, A. A. Haghighirad, N. R. Davies, A. McCollam, A. Narayanan, S. F. Blake, Y. L. Chen, S. Ghannadzadeh, A. J. Schofield, M. Hoesch, C. Meingast, T. Wolf, and A. I. Coldea, “Emergence of the nematic electronic state in FeSe,” *Phys. Rev. B* **91**, 155106 (2015).
- [22] V. Brouet, D. LeBoeuf, P.-H. Lin, J. Mansart, A. Taleb-Ibrahimi, P. Le Fevre, F. Bertran, A. Forget, and D. Colson, “ARPES view of orbitally resolved quasiparticle lifetimes in iron pnictides,” *Phys. Rev. B* **93**, 085137 (2016).
- [23] L. Stojchevska, T. Mertelj, J.-H. Chu, I. R. Fisher, and D. Mihailovic, “Doping dependence of femtosecond quasiparticle relaxation dynamics in Ba(Fe_{1-x}Co_x)₂As₂ single crystals: Evidence for normal-state nematic fluctuations,” *Phys. Rev. B* **86**, 024519 (2012).
- [24] H. Suzuki, K. Okazaki, T. Yamamoto, T. Someya, M. Okada, K. Koshiishi, M. Fujisawa, T. Kanai, N. Ishii, M. Nakajima, H. Eisaki, K. Ono, H. Kumigashira, J. Itatani, A. Fujimori, and S. Shin, “Ultrafast melting of spin density wave order in BaFe₂As₂ observed by time- and angle-resolved photoemission spectroscopy with extreme-ultraviolet higher harmonic generation,” *Phys. Rev. B* **95**, 165112 (2017).
- [25] P.-T. Dong and J.-X. Cheng, “Pump–probe microscopy: theory, instrumentation, and applications,” *Spectroscopy* **32**(4), 24–36 (2017).
- [26] J.-C. Diels and W. Rudolph, *Ultrashort Laser Pulse Phenomena*, 2nd ed. (Academic Press, 2006).
- [27] A. L. Trinh and A. Esposito, “Biochemical resolving power of fluorescence lifetime imaging: untangling the roles of the instrument response function and photon-statistics,” *Biomed. Opt. Express* **12**(7), 3775–3788 (2021).
- [28] G. Casella and R. L. Berger, *Statistical Inference*, 2nd ed. (Duxbury, Pacific Grove, CA, 2002).
- [29] T. Qiu and C. Tien, “Femtosecond laser heating of multilayer metals – I. Analysis,” *Int. J. Heat Mass Transfer* **37**, 2789–2797 (1994).
- [30] P. M. Norris, A. P. Caffrey, R. J. Stevens, J. M. Klopff, J. T. McLeskey, and A. N. Smith, “Femtosecond pump–probe nondestructive examination of materials (invited),” *Rev. Sci. Instrum.* **74**, 400–406 (2003).
- [31] A. N. Smith and P. M. Norris, “Influence of intraband transitions on the electron thermoreflectance response of metals,” *Appl. Phys. Lett.* **78**, 1240–1242 (2001).
- [32] S. B. Naldo, A. V. Bernotas, and B. F. Donovan, “Understanding the sensitivity of the two-temperature model for electron–phonon coupling measurements,” *J. Appl. Phys.* **128**, 085102 (2020).
- [33] D. L. Maslov, A. V. Chubukov, “Optical response of correlated electron systems,” *Rep. Prog. Phys.* **80**, 026503 (2016).
- [34] R. N. Gurzhi, “Mutual electron correlations in metal optics,” *Sov. Phys. JETP* **8**, 673 (1959).
- [35] T. Suzuki, Y. Kubota, A. Nakamura, T. Shimojima, K. Takubo, S. Ito, K. Yamamoto, S. Michimae, H. Sato, H. Hiratsuka, *et al.*, “Ultrafast optical stress on BaFe₂As₂,” *Phys. Rev. Res.* **3**, 033222 (2021).

SUPPLEMENTARY MATERIAL

INSTRUMENT RESPONSE FUNCTION CORRECTION IN THE NEMATIC RESPONSE FUNCTION MODEL

1. Definitions

We model the intrinsic material response as

$$f(t; \tau) = \begin{cases} 1, & t < 0, \\ e^{-t/\tau}, & t \geq 0, \end{cases} \quad (24)$$

which can be written using the Heaviside step function $H(t)$ as

$$f(t; \tau) = 1 - H(t)(1 - e^{-t/\tau}) = 1 - H(t) + H(t)e^{-t/\tau}. \quad (25)$$

The instrument response function (IRF) in a pump-probe measurement is the cross-correlation of the pump and probe pulses which characterizes the time resolution of the experiment [1, 2]. For Gaussian pump and probe pulses of equal duration τ_p at the full width at half maximum (FWHM), the IRF is also Gaussian, with FWHM $\tau_{\text{IRF}} = \sqrt{2}\tau_p$. The corresponding root-mean-square (RMS) width σ is [1, 2]:

$$\sigma \equiv \frac{\tau_{\text{IRF}}}{2\sqrt{2\ln 2}} = \frac{\tau_{\text{IRF}}}{\kappa}, \quad \kappa \equiv 2\sqrt{2\ln 2}. \quad (26)$$

The normalized Gaussian IRF is then

$$g(t) = \frac{1}{\sqrt{2\pi}\sigma} \exp\left(-\frac{t^2}{2\sigma^2}\right), \quad \int_{-\infty}^{\infty} g(t) dt = 1, \quad (27)$$

The measured (convolved) signal is

$$F(t; \tau) = (g * f)(t) = \int_{-\infty}^{\infty} g(t-u) f(u; \tau) du. \quad (28)$$

2. Explicit form of the convolved single-channel trace

Inserting Eq. (25) into Eq. (28) yields

$$F(t; \tau) = (g * 1)(t) - (g * H)(t) + (g * (He^{-t/\tau}))(t). \quad (29)$$

Because g is normalized, $(g * 1)(t) = 1$, hence

$$F(t; \tau) = 1 - (g * H)(t) + S(t; \tau, \sigma), \quad (30)$$

where we define

$$S(t; \tau, \sigma) \equiv (g * (He^{-t/\tau}))(t) = \int_0^{\infty} g(t-u) e^{-u/\tau} du. \quad (31)$$

The convolution with the step function is

$$(g * H)(t) = \int_0^{\infty} g(t-u) du = \int_{-\infty}^t g(w) dw = \Phi\left(\frac{t}{\sigma}\right), \quad (32)$$

where Φ is the standard normal cumulative distribution function (CDF) [3]

$$\Phi(x) = \int_{-\infty}^x \phi(t) dt, \quad \phi(t) = \frac{1}{\sqrt{2\pi}} e^{-t^2/2}. \quad (33)$$

Inserting Eq. (27) into Eq. (31):

$$S(t; \tau, \sigma) = \int_0^\infty \frac{1}{\sqrt{2\pi}\sigma} \exp\left[-\frac{(t-u)^2}{2\sigma^2} - \frac{u}{\tau}\right] du. \quad (34)$$

Expanding the exponent and defining $\mu \equiv t - \sigma^2/\tau$, we obtain

$$S(t; \tau, \sigma) = \exp\left(\frac{\sigma^2}{2\tau^2} - \frac{t}{\tau}\right) \int_0^\infty \frac{1}{\sqrt{2\pi}\sigma} \exp\left[-\frac{(u-\mu)^2}{2\sigma^2}\right] du. \quad (35)$$

With the substitution $y = (u - \mu)/\sigma$, the integral yields

$$\int_0^\infty \frac{1}{\sqrt{2\pi}\sigma} \exp\left[-\frac{(u-\mu)^2}{2\sigma^2}\right] du = \int_{(-\mu)/\sigma}^\infty \phi(y) dy = \Phi\left(\frac{\mu}{\sigma}\right). \quad (36)$$

Since $\mu/\sigma = t/\sigma - \sigma/\tau$, we obtain

$$\boxed{S(t; \tau, \sigma) = \exp\left(\frac{\sigma^2}{2\tau^2} - \frac{t}{\tau}\right) \Phi\left(\frac{t}{\sigma} - \frac{\sigma}{\tau}\right)}. \quad (37)$$

Combining Eqs. (30), (32), and (37):

$$\boxed{F(t; \tau) = 1 - \Phi\left(\frac{t}{\sigma}\right) + S(t; \tau, \sigma)}, \quad (38)$$

where σ is related to τ_{IRF} by Eq. (26). For $t \gg \sigma$, $\Phi(t/\sigma) \approx 1$, so $F(t; \tau) \approx S(t; \tau, \sigma)$.

3. Nematic response function and small-anisotropy expansion

We define

$$\eta(t) \equiv F(t; \tau_{\parallel}) - F(t; \tau_{\perp}), \quad \Delta_{\tau} \equiv \tau_{\perp} - \tau_{\parallel}, \quad \tau \equiv \tau_{\text{avg}} \equiv \frac{\tau_{\parallel} + \tau_{\perp}}{2}. \quad (39)$$

Equivalently, $\tau_{\parallel} = \tau - \Delta_{\tau}/2$ and $\tau_{\perp} = \tau + \Delta_{\tau}/2$. For $\Delta_{\tau} > 0$, $\eta(t)$ has a minimum with $\eta_{\text{min}} < 0$. Using Eq. (38), the terms $1 - \Phi(t/\sigma)$ cancel out, yielding

$$\eta(t) = S(t; \tau_{\parallel}, \sigma) - S(t; \tau_{\perp}, \sigma). \quad (40)$$

For $|\Delta_{\tau}| \ll \tau$, a first-order Taylor expansion of Eq. (40) gives

$$S\left(\tau - \frac{\Delta_{\tau}}{2}\right) - S\left(\tau + \frac{\Delta_{\tau}}{2}\right) \approx -\Delta_{\tau} \frac{\partial S}{\partial \tau}(t; \tau, \sigma), \quad (41)$$

so

$$\boxed{\eta(t) \approx -\Delta_{\tau} \partial_{\tau} S(t; \tau, \sigma)}. \quad (42)$$

An extremum of $\eta(t)$ satisfies $d\eta/dt = 0$. Assuming $\Delta_{\tau} \neq 0$,

$$\boxed{\partial_{t\tau} S(t_{\text{min}}; \tau, \sigma) = 0}. \quad (43)$$

4. Derivation of corrections to t_{min}

Rewriting Eq. (37) as

$$S(t; \tau, \sigma) = e^A \Phi(x), \quad A = \frac{\sigma^2}{2\tau^2} - \frac{t}{\tau}, \quad x = \frac{t}{\sigma} - \frac{\sigma}{\tau}. \quad (44)$$

Note $\Phi'(x) = \phi(x)$, and ϕ is given in Eq. (33).

First derivative with respect to t yields

$$\begin{aligned}\partial_t S &= e^A \left[(\partial_t A) \Phi(x) + \Phi'(x) \partial_t x \right] \\ &= e^A \left[-\frac{\Phi(x)}{\tau} + \frac{\phi(x)}{\sigma} \right],\end{aligned}\quad (45)$$

since $\partial_t A = -1/\tau$ and $\partial_t x = 1/\sigma$.

We differentiate Eq. (45) with respect to τ . Defining

$$M \equiv -\frac{\Phi(x)}{\tau} + \frac{\phi(x)}{\sigma}, \quad \partial_t S = e^A M. \quad (46)$$

Then

$$\partial_{t\tau} S = \partial_\tau (e^A M) = e^A \left[(\partial_\tau A) M + \partial_\tau M \right]. \quad (47)$$

Because $e^A > 0$, Eq. (43) is equivalent to

$$(\partial_\tau A) M + \partial_\tau M = 0. \quad (48)$$

The auxiliary derivatives:

$$\partial_\tau A = -\frac{\sigma^2}{\tau^3} + \frac{t}{\tau^2}, \quad \partial_\tau x = \frac{\sigma}{\tau^2}. \quad (49)$$

To compute $\partial_\tau M$, we will separately evaluate the derivatives of two terms from Eq. (46). Taking the derivative of the first term,

$$\partial_\tau \left(-\frac{\Phi(x)}{\tau} \right) = \frac{\Phi(x)}{\tau^2} - \frac{1}{\tau} \phi(x) \partial_\tau x = \frac{\Phi(x)}{\tau^2} - \frac{\sigma \phi(x)}{\tau^3}. \quad (50)$$

For the second term, using $\phi'(x) = -x\phi(x)$,

$$\partial_\tau \left(\frac{\phi(x)}{\sigma} \right) = \frac{1}{\sigma} \phi'(x) \partial_\tau x = \frac{1}{\sigma} (-x\phi(x)) \frac{\sigma}{\tau^2} = -\frac{x\phi(x)}{\tau^2}. \quad (51)$$

Thus

$$\partial_\tau M = \frac{\Phi(x)}{\tau^2} - \frac{\sigma \phi(x)}{\tau^3} - \frac{x\phi(x)}{\tau^2}. \quad (52)$$

Substituting Eqs. (46), (49), and (52) into Eq. (48), multiplying by τ^3 , then simplifying using $x = t/\sigma - \sigma/\tau$ yields:

$$\boxed{\left(\tau + \frac{\sigma^2}{\tau} - t \right) \Phi(x) = \sigma \phi(x), \quad x = \frac{t}{\sigma} - \frac{\sigma}{\tau}.} \quad (53)$$

Rearranging Eq. (53) gives

$$t = \tau + \frac{\sigma^2}{\tau} - \sigma \frac{\phi(x)}{\Phi(x)} = \tau + \frac{\sigma^2}{\tau} - \sigma \Lambda(x), \quad (54)$$

where $\Lambda(x)$ is the inverse Mills ratio [4],

$$\boxed{\Lambda(x) \equiv \frac{\phi(x)}{\Phi(x)}.} \quad (55)$$

Therefore,

$$\boxed{t_{\min} = \tau + \frac{\sigma^2}{\tau} - \sigma \Lambda(x), \quad x = \frac{t_{\min}}{\sigma} - \frac{\sigma}{\tau}.} \quad (56)$$

5. Explicit approximation in terms of τ_{IRF}

As a first approximation, we neglect the $\sigma\Lambda(x)$ term in Eq. (56):

$$t_{\min}^{(0)} = \tau + \frac{\sigma^2}{\tau}. \quad (57)$$

Inserting Eq. (57) into the definition of x :

$$x^{(0)} = \frac{t_{\min}^{(0)}}{\sigma} - \frac{\sigma}{\tau} = \frac{1}{\sigma} \left(\tau + \frac{\sigma^2}{\tau} \right) - \frac{\sigma}{\tau} = \frac{\tau}{\sigma}. \quad (58)$$

Using Eq. (26), this becomes

$$\boxed{x^{(0)} = \frac{\tau}{\sigma} = \frac{\kappa \tau}{\tau_{\text{IRF}}}.} \quad (59)$$

Hence an explicit approximation (a one-step fixed-point iteration) is

$$\boxed{t_{\min} \approx \tau + \frac{\sigma^2}{\tau} - \sigma\Lambda\left(\frac{\tau}{\sigma}\right) = \tau + \frac{\tau_{\text{IRF}}^2}{\kappa^2\tau} - \frac{\tau_{\text{IRF}}}{\kappa} \Lambda\left(\frac{\kappa\tau}{\tau_{\text{IRF}}}\right).} \quad (60)$$

If $u \equiv \tau/\sigma = \kappa\tau/\tau_{\text{IRF}} > 3$, then $\Phi(u) \approx 1$ and $\Lambda(u) \approx \phi(u) \propto e^{-u^2/2}$ is exponentially small, giving

$$\boxed{t_{\min} \approx \tau + \frac{\sigma^2}{\tau} = \tau + \frac{\tau_{\text{IRF}}^2}{\kappa^2\tau} \quad \left(\frac{\kappa\tau}{\tau_{\text{IRF}}} > 3 \right).} \quad (61)$$

For an experimentally relevant case ($\tau_{\text{IRF}} = 50$ fs and $\tau \approx 100$ fs), the difference between τ obtained from the full implicit extremum condition (Eq. (56), evaluated numerically) and the estimate based on Eq. (61) is below 5 fs (Fig. 1(f) of the main text). Here $\sigma = \tau_{\text{IRF}}/\kappa \approx 21$ fs, so $u \equiv \tau/\sigma \approx 4.7 > 3$, which satisfies the condition used in Eq. (61).

6. Derivation of the minimum amplitude η_{\min} for $u = \kappa\tau/\tau_{\text{IRF}} > 3$

For $u > 3$ and $t \gtrsim 0$, $\Phi(x) \approx 1$ near the extremum, so Eq. (37) simplifies to

$$S(t; \tau, \sigma) \approx \exp\left(\frac{\sigma^2}{2\tau^2} - \frac{t}{\tau}\right) = \exp\left(\frac{\tau_{\text{IRF}}^2}{2\kappa^2\tau^2} - \frac{t}{\tau}\right). \quad (62)$$

Differentiating Eq. (62) with respect to τ :

$$\begin{aligned} \partial_{\tau} S &= S \cdot \partial_{\tau} \left(\frac{\sigma^2}{2\tau^2} - \frac{t}{\tau} \right) \\ &= S \left(-\frac{\sigma^2}{\tau^3} + \frac{t}{\tau^2} \right) = S \left(-\frac{\tau_{\text{IRF}}^2}{\kappa^2\tau^3} + \frac{t}{\tau^2} \right). \end{aligned} \quad (63)$$

From Eq. (42),

$$\eta(t) \approx -\Delta_{\tau} S(t; \tau, \sigma) \left(-\frac{\sigma^2}{\tau^3} + \frac{t}{\tau^2} \right) = -\Delta_{\tau} S(t; \tau, \sigma) \left(-\frac{\tau_{\text{IRF}}^2}{\kappa^2\tau^3} + \frac{t}{\tau^2} \right). \quad (64)$$

Using Eq. (61), the bracket becomes

$$\begin{aligned} -\frac{\sigma^2}{\tau^3} + \frac{t_{\min}}{\tau^2} &\approx -\frac{\sigma^2}{\tau^3} + \frac{1}{\tau^2} \left(\tau + \frac{\sigma^2}{\tau} \right) \\ &= -\frac{\sigma^2}{\tau^3} + \frac{1}{\tau} + \frac{\sigma^2}{\tau^3} = \frac{1}{\tau}, \end{aligned} \quad (65)$$

therefore

$$\eta_{\min} \approx -\Delta_{\tau} \frac{1}{\tau} S(t_{\min}; \tau, \sigma). \quad (66)$$

Evaluating $S(t_{\min})$ using Eq. (62) and $t_{\min} \approx \tau + \sigma^2/\tau$:

$$\begin{aligned} S(t_{\min}) &\approx \exp\left(\frac{\sigma^2}{2\tau^2} - \frac{1}{\tau} \left(\tau + \frac{\sigma^2}{\tau}\right)\right) \\ &= \exp\left(\frac{\sigma^2}{2\tau^2} - 1 - \frac{\sigma^2}{\tau^2}\right) = e^{-1} e^{-\sigma^2/(2\tau^2)} \\ &= e^{-1} \exp\left(-\frac{\tau_{\text{IRF}}^2}{2\kappa^2\tau^2}\right). \end{aligned} \quad (67)$$

Inserting Eq. (67) into Eq. (66):

$$\boxed{\eta_{\min} \approx -\frac{\Delta_{\tau}}{e\tau} \exp\left(-\frac{\tau_{\text{IRF}}^2}{2\kappa^2\tau^2}\right) \quad \left(\frac{\kappa\tau}{\tau_{\text{IRF}}} > 3\right)}. \quad (68)$$

7. Convolution-corrected results for finite τ_{IRF}

For equal amplitudes ($r = 1$) and $|\Delta_{\tau}| \ll \tau$:

$$\boxed{t_{\min} \approx \tau + \frac{\tau_{\text{IRF}}^2}{\kappa^2\tau} \quad \left(\frac{\kappa\tau}{\tau_{\text{IRF}}} > 3\right)}. \quad (69)$$

From Eq. (68),

$$\boxed{\Delta_{\tau} \approx -e\eta_{\min}\tau \exp\left(\frac{\tau_{\text{IRF}}^2}{2\kappa^2\tau^2}\right) \quad \left(\frac{\kappa\tau}{\tau_{\text{IRF}}} > 3\right)}. \quad (70)$$

Solving Eq. (69) for $\tau \equiv \tau_{\text{avg}}$:

$$t_{\min}\tau = \tau^2 + \frac{\tau_{\text{IRF}}^2}{\kappa^2} \Rightarrow \tau^2 - t_{\min}\tau + \frac{\tau_{\text{IRF}}^2}{\kappa^2} = 0, \quad (71)$$

so

$$\boxed{\tau \approx \frac{t_{\min} + \sqrt{t_{\min}^2 - 4(\tau_{\text{IRF}}^2/\kappa^2)}}{2}}. \quad (72)$$

For $\kappa t_{\min}/\tau_{\text{IRF}} \gg 1$, a simpler approximation is

$$\boxed{\tau \approx t_{\min} - \frac{\tau_{\text{IRF}}^2}{\kappa^2 t_{\min}} = t_{\min} - \frac{\tau_{\text{IRF}}^2}{8 \ln(2) t_{\min}}}. \quad (73)$$

-
- [1] J.-C. Diels and W. Rudolph, *Ultrashort Laser Pulse Phenomena*, 2nd ed. (Academic Press, 2006).
 [2] B. E. A. Saleh and M. C. Teich, *Fundamentals of Photonics*, 2nd ed. (Wiley, 2007).
 [3] G. Casella and R. L. Berger, *Statistical Inference*, 2nd ed. (Duxbury, Pacific Grove, CA, 2002).
 [4] I. Pinelis, "Exact bounds on the inverse Mills ratio and its derivatives," *Complex Analysis and Operator Theory* **13**(4), 1643–1651 (2019).